ELSEVIER

Journal of Applied Geophysics 49 (2002) 111–127

JOURNAL OF APPLIED GEOPHYSICS

www.elsevier.com/locate/jappgeo

Finite-difference modeling of borehole ground penetrating radar data

Deming Wang, George A. McMechan*

Center for Lithospheric Studies, The University of Texas at Dallas, 2601 N. Floyd Road (Fa31), PO Box 830688, Richardson, TX 75083-0688, USA

Received 26 July 2000; accepted 7 August 2001

Abstract

In the fall of 1996, borehole ground penetrating radar (BGPR) data were acquired as part of a comprehensive characterization of a clastic reservoir analog in the Ferron Sandstone in east central Utah. BGPR data were collected in and between three 15-m-deep holes as well as surface profiles that connect each pair of holes. Two-dimensional finite-difference modeling of the data provides estimates of the distributions of velocity and attenuation, and the geometry of the reflectors. Depth control on the interfaces in the model is provided by the core logs from the three holes. Average estimated relative dielectric permittivity generally increases with depth from ~ 4 to ~ 17 in the sandy units, and is larger (as high as ~ 30) in the clays. The corresponding estimated electrical conductivities are from 10^{-8} S/m for the most sandy layers to 10^{-2} S/m for the most clay-rich layers. Comparing the velocities for vertical and horizontal electric field propagations shows a 20–25% anisotropy in the upper 6–7 m; vertical propagation (with horizontal polarization) is faster than horizontal propagation (with vertical polarization). This anisotropy is interpreted as being caused by the pervasive vertically oriented conjugate fractures that are visible at the site. At greater depths, the anisotropy is not seen, which we interpret as smaller fracture widths below the depths affected by surface weathering.

Keywords: Ground-penetrating radar (GPR); Borehole data; Finite-difference modeling; Wavefields

1. Introduction

Detailed characterizations of the internal structures of aquifers and reservoirs are an important part of most engineering and environmental site evaluations, and of reservoir analog studies. A reservoir analog is a surface exposure of a unit that has lithology and a sedimentary environment that is similar to that of a real reservoir or acquifer. The value of an analog results from the fact that it is accessible for study, unlike a real reservoir that may be deeply buried. In the past, such models have typically been constructed from one-dimensional (1-D) profiles at coreholes, or from two-dimensional (2-D) data where sufficient geologic information is exposed at the surface. At best, these approaches involve assumptions of continuity that are the basis of interpolation and extrapolation of features observed at the control points. Such assumptions may not be accurate. Thus, it is desirable to have a method of directly constraining the geologic model between holes and outcrops; one economical way to do this,

* Corresponding author.
E-mail address: mcmec@utdallas.edu (G.A. McMechan).

0926-9851/02/$ - see front matter
PII: S0926-9851(01)00092-1

for shallow environments, is with surface ground-penetrating radar (GPR) surveys, and borehole ground penetrating radar (BGPR) surveys.

Good summaries of the GPR method are given by Daniels et al. (1988), Davis and Annan (1989), Daniels (1996), and Reynolds (1997); BGPR is described by Olhoeft (1988) and Olsson et al. (1992). BGPR data are usually acquired well below the earth's surface to avoid complications generated at the air–earth interface (Siggins, 1992), but the complementary use of both surface and BGPR data has advantages as they provide independent constraints (Holloway et al., 1992) on reflector geometry and on depths and velocities, respectively. GPR has previously been used for site characterization in both clastic and carbonate environments (Gawthorpe et al., 1993; McMechan et al., 1997; Corbeanu et al., in press; Szerbiak et al., in press; Loucks et al., 2001).

As part of a multi-disciplinary characterization of a reservoir analog in east central Utah in 1996, we acquired BGPR data in, and between, three cored boreholes. The survey geometries include vertical radar profiles in each of the three holes, constant-depth (horizontal propagation) profiles between each of the three pairs of holes, tomographic sweeps between sources in one hole and receivers in the other hole and along the surface, and surface common-offset GPR profiles connecting the three holes. While a variety of additional data were collected, we concentrate in this paper on analysis of the borehole-related GPR data; this interdisciplinary approach is unique, and has analysis of the BGPR data as a prerequisite. We use numerical modeling as this provides the most reliable identification of each GPR wave type, and so is a solid foundation for interpretation. Other aspects of the project (3-D GPR data imaging, sedimentological interpretation, integration with lab measurements) are presented elsewhere (Corbeanu et al., in press; Szerbiak et al., in press; McMechan and Soegaard, 1998). The trends and average values in the model developed below are guided by the lab measurements (see McMechan and Soegaard, 1998).

2. 2-D finite-difference GPR modeling

A variety of methods are available for numerical synthesis of GPR data. These include ray-based methods (Goodman, 1994; Cai and McMechan, 1995), transform methods (Zeng et al., 1995), integral methods (Ellefsen, 1999), and finite-difference methods (Xu and McMechan, 1997; Bergmann et al., 1999; Holliger and Bergmann, 1999).

A simplification of the 2.5-D second-order finite-difference time/space domain solution of Maxwell's equations by Xu and McMechan (1997) is used for the modeling presented below. The air–earth interface is included by defining the upper layer in the model to be air (Fig. 1), and all four sides of the model grids have absorbing boundary conditions implemented with a combination of the wavefield tapering algorithm of Cerjan et al. (1985) and the second order algorithm of Mur (1981). All models are 2.5-D; that is the structures are defined on a vertical 2-D plane and this structure is assumed to be invariant perpendicular to this plane. The coordinate system is (x, y, z) = (horizontal in-plane, horizontal out-of-plane, depth). Instead of superimposing solutions for multiple horizontal wave numbers to simulate a (3-D) point dipole source rather than a line (2-D) source (Xu and McMechan, 1997), the field data amplitudes are scaled by $t^{0.5}$, where t is the total travel-time (Crase et al., 1990). This corrects approximately for the difference between the 2-D (line source) and 3-D (point source) geometrical spreading; pulse shapes are not adjusted, but this is not crucial for the type of analysis done below. We are interested mainly in reproducing the observed traveltime behavior of the reflections, along with approximate amplitudes; wavelet shape changes and details such as dispersion are of less interest.

The directivity of the transmitter radiation patterns and the corresponding directional sensitivity of the receiving antenna are a consequence of their respective dipole orientations, and the interaction of the dipole wavefields with the boundary conditions at their respective locations in the model. Thus, an antenna buried (in a borehole) has the same dipole radiation (or directional response) pattern regardless of whether the antenna is transmitting or receiving. Similarly, at the air–earth interface, the directionality of an antenna with a specific orientation is the same regardless of whether the antenna is transmitting or receiving because of the interaction of the up- and down-going waves at the interface; the corresponding boundary conditions are automatically and implicitly

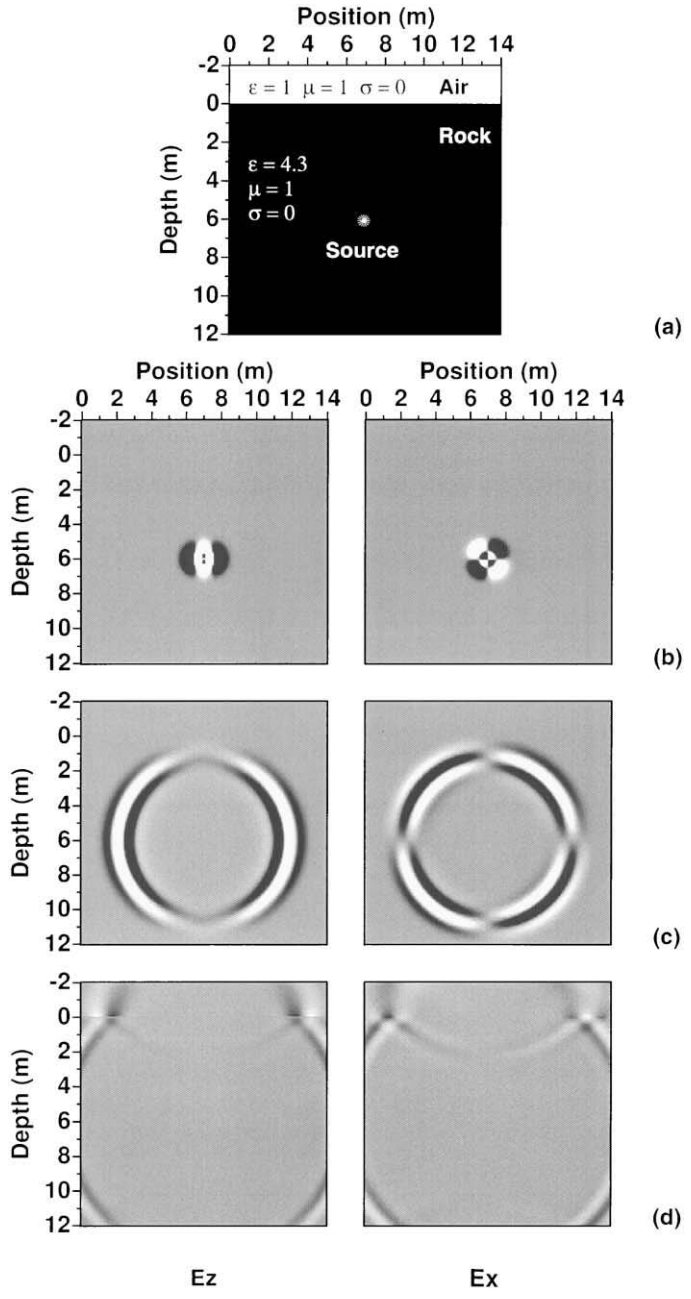

Fig. 1. Radiation pattern and propagation for a vertical dipole source in a homogeneous layer. ε and μ are the relative dielectric permittivity, and relative magnetic permeability, respectively; electrical conductivity (σ) is in S/m. (a) is the model. (b), (c), and (d) are snapshots at 16, 48, and 72 ns. The left and right panels of each pair are the vertical and the (in-plane) horizontal electric fields (E_z and E_x), respectively.

applied in a finite-difference solution. Thus, for example, if we choose to extract a horizontally polarized field at the air–earth interface, the directional properties are implicit via superposition of the incident and reflected (or critically refracted) waves. The numerical implementation of the oriented sources is

via the ohmic current term in Maxwell's equation [see *J* in Eq. (1) of Keller, 1987, or in Eq. (1b) of Xu and McMechan, 1997].

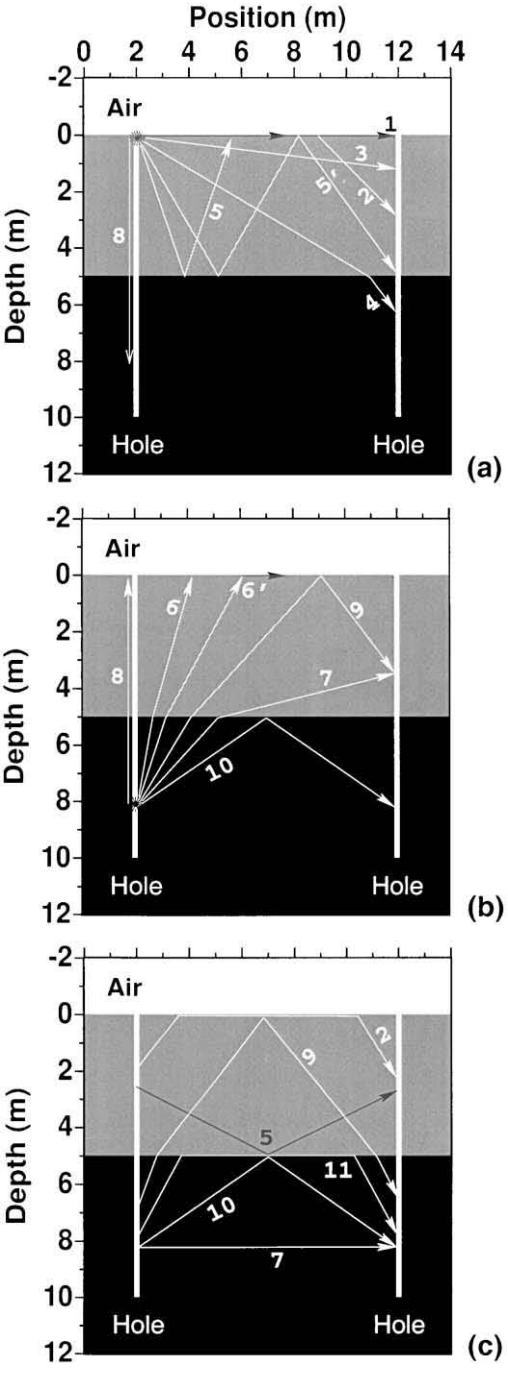

Table 1
Electromagnetic properties for the layered media

	Air	Upper layer	Halfspace (case 1)	Halfspace (case 2)
Dielectric	1	8	12	12
Magnetic permeability	1	1	1	1
DC conductivity (S/m)	0	0	0	0.008

The model is parameterized in terms of only two quantities; the relative dielectric permittivity (referred to below as the dielectric constant), which controls the propagation velocity, and electrical conductivity, which controls the attenuation. Reflections are assumed to be generated by contrasts in dielectric constant and in electrical conductivity. The earth is assumed to be non-magnetic, which is reasonable in this environment.

The field GPR data were all collected with what were nominally 100 MHz antennas; however, the actual spectra of the recorded data peak near 50 MHz. Thus, the numerical modeling was performed with a bandlimited (Ricker) time wavelet with a dominant frequency of 50 MHz. For antennas on the earth's surface (for all survey geometries except the constant offset surface survey), we simulate transmission or receiving signals with dipoles oriented horizontally, in the plane of the 2-D model (the *x*-direction); antennas in the boreholes are oriented vertically within the model plane (the *z*-direction); for the surface surveys, the antennas are oriented horizontally and perpendicular to the model plane (the *y*-direction). These correspond to the field recording geometries. The boreholes themselves are not included in the model; they are assumed to be of diameter much smaller than a wavelength (which is true for all the data considered), and so are not expected to play a major role in the response.

Fig. 2. Model consisting of a rock layer between two half spaces [air (above) and rock (below)]; parameters are given in Table 1. The stars at 0.0- and 8.0-m depths in (a) and (b) are the source locations for the synthetic responses in (Figs. 3, 4 and 6a,b). Numbered propagation paths correspond to the similarly numbered wave fronts in Figs. 3–6.

The grid dimensions used in the numerical simulations vary with the specific computation being done, but in all cases, the grid increment in both horizontal and vertical coordinates is 5 cm which, assuming a maximum usable frequency of 150 MHz, is ~40 grid points per wavelength in the air, which, with a time

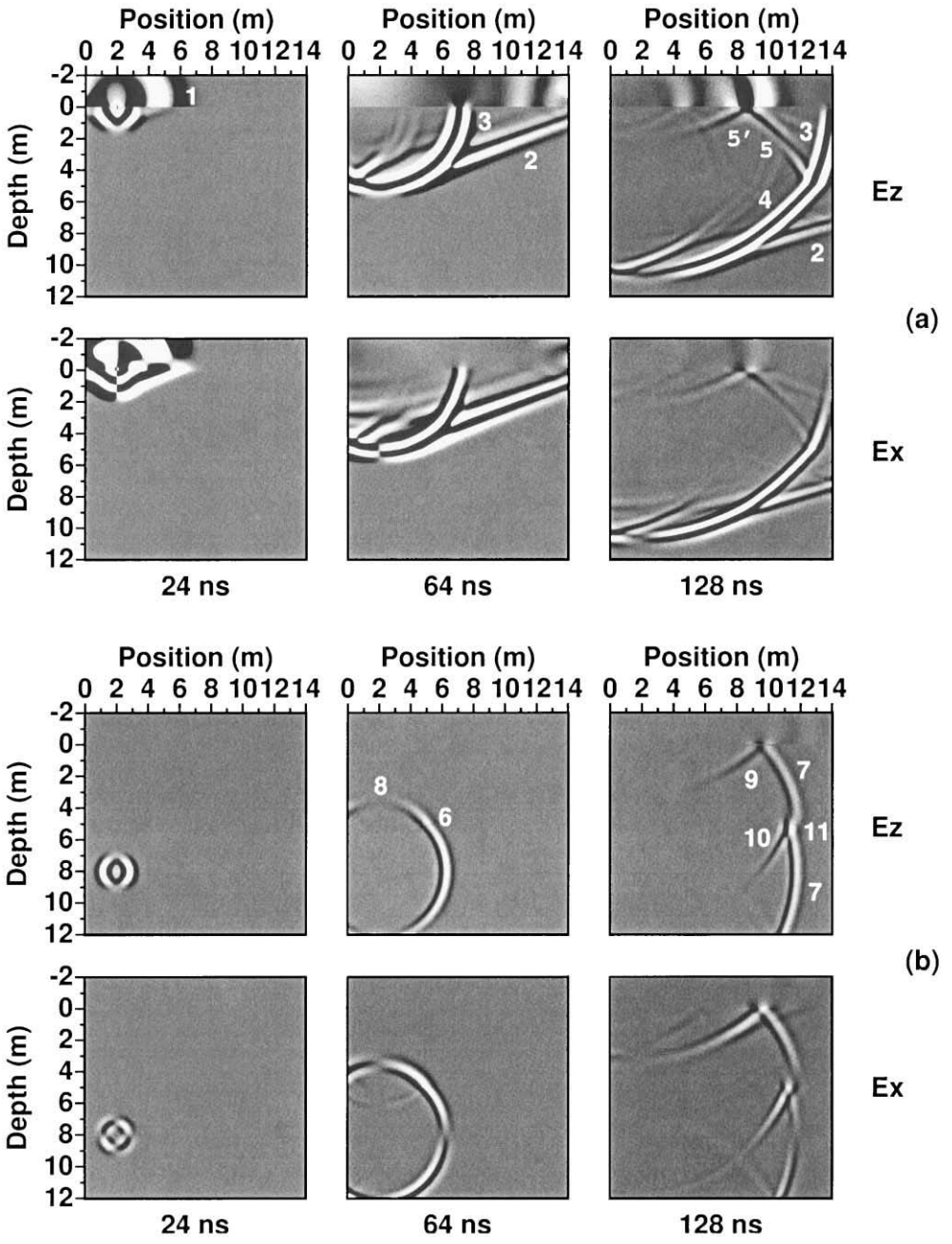

Fig. 3. Fixed-time snapshots for waves propagating in the model shown in Fig. 2. (a) are for a source at the surface; (b) are for a source at 8-m depth. Numbers next to the wave fronts identify the paths with the same numbers in Fig. 2. Snapshot times are given below each pair of plots.

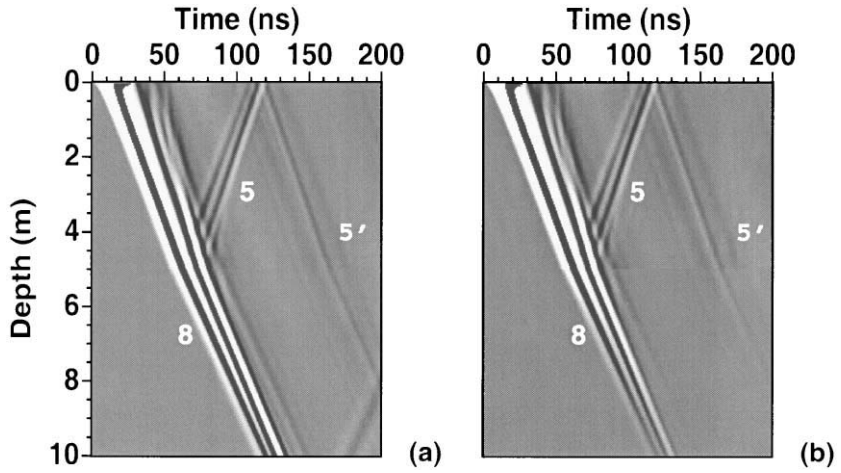

Fig. 4. Vertical E_z GPR profiles, (a) without and (b) with attenuation in the lower halfspace of the model in Fig. 2. Labeled arrivals correspond to those similarly labeled in Figs. 2 and 3.

step of 0.1 ns, satisfies the grid dispersion and stability requirements (Petropolis, 1994).

3. Synthetic examples

To illustrate the main features expected in BGPR data, this section contains some salient examples for models and recording geometries of progressively increasing complexity. Similar features are seen in the field data shown in the following section.

3.1. Propagation in a homogeneous model

Fig. 1a shows a model composed of two homogeneous halfspaces (air and earth) and the location of a buried vertical dipole source. The other panels in Fig. 1 show the vertical (E_z) and horizontal (E_x) electric fields for the response of the model to this source at three times. The expected dipole radiation pattern is clearly visible, as is the reflection from the air–earth interface, and the action of the absorbing boundary conditions.

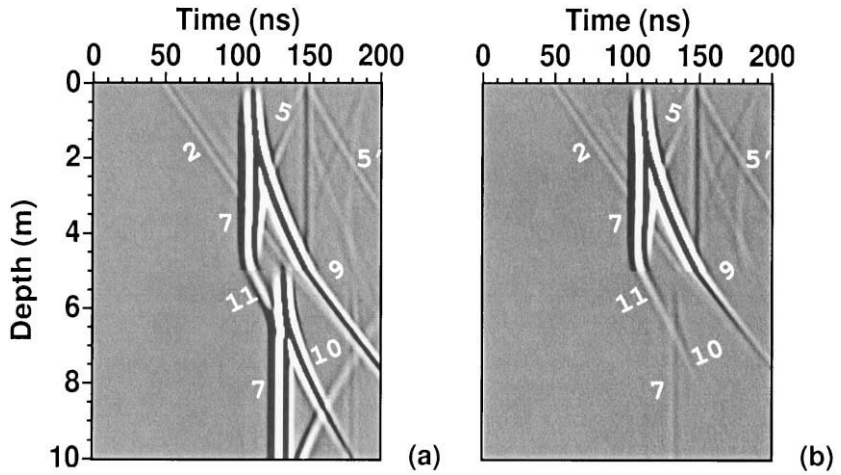

Fig. 5. Common-depth E_z profiles between the two holes in the model in Fig. 2 (a) without and (b) with attenuation in the lower halfspace. Labeled arrivals correspond to those similarly labeled in Figs. 2 and 3.

3.2. Propagation in a layered model

Fig. 2 contains a two-layers-over-a-halfspace earth model and numbered ray path trajectories for the main arrivals generated by dipole sources at the surface (Fig. 2a), at 8-m depth (Fig. 2b), and for a few representative constant-depth survey points (Fig. 2c). The ray path numbers correspond to the numbered wave fronts in Figs. 3–6. Properties of non-attenuating and attenuating versions ('case 1' and 'case 2', respectively) of this

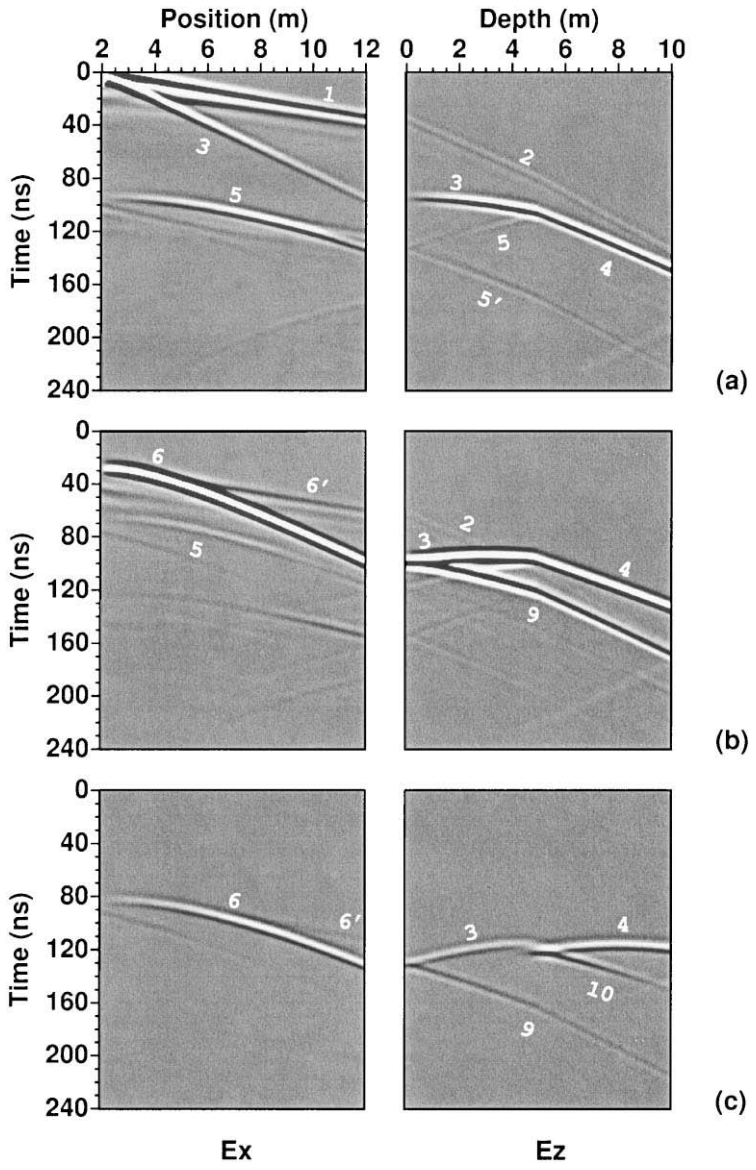

Fig. 6. Common-source tomographic profiles for transmitters located at three depths in the left borehole in the model in Fig. 2. (a) is for 0-m depth; (b) is for 3-m depth; (c) is for 8-m depth. For all three, the transmitters are at 2.0 m on the horizontal axis in Fig. 2. For each of (a), (b) and (c), the left panel of each pair is for receivers along the earth's surface; the right panel is the E_z field for receivers down the right borehole. Labeled arrivals correspond to those similarly labeled in Figs. 2 and 3.

model are given in Table 1. Fig. 3a and b shows the wave fronts present in three fixed-time snapshots in the non-attenuating version of the model, generated by the surface source and deep sources, respectively. Direct and reflected waves are clearly visible in both the E_z and E_x wavefields. Recording of these and related waves in various BGPR acquisition geometries are illustrated in the next figures.

Fig. 4 shows a comparison of two synthetic vertical GPR profiles in one of the two holes in the model in Fig. 2 to illustrate a typical layered model response. A vertical GPR profile contains the traces, recorded at a series of equally spaced points within a borehole, generated by a transmitting antenna at the top of the hole (or with the role of the two antennas reversed). Fig. 4 shows the effect of high conductivity in the lower half-space both in increasing attenuation in the half-space, and increasing the reflectivity at the layer-to-halfspace boundary; compare amplitudes labeled 8 and 5, respectively. Multiples (5′) between the air–earth surface and the layer bottom are also clearly visible.

Fig. 5 shows the synthetic common-depth profiles between the two holes in the attenuating and non-attenuating versions of the model in Fig. 2. In these profiles, each trace corresponds to a single transmitter antenna in one hole and a single receiver antenna at the same depth in the other hole. Each trace is recorded at a different antenna depth. The common-depth profiles (Fig. 5) contain direct waves (labeled 7) between the holes, critically refracted air waves (labeled 2) at the air–earth interface, and internal reflections and refractions (labeled 5, 9, 10, and 11).

Fig. 6 shows representative synthetic tomographic profiles. Each tomographic profile contains all the traces for a single transmitter position in one hole, recorded at equally spaced receivers that span the entire depth interval of the other hole (the right panels), and across the earth's surface between the two holes (the left panels). The fields plotted in the left panels (E_x) and the right panels (E_z) correspond to those recorded in the field data (presented below). The rightmost trace of each left panel and the leftmost trace of the corresponding right panel are both recorded at the same location (at the top of the right borehole), but, as they are the E_x and E_z fields, they have systematically different amplitudes and phases. There is a gradual progression of the arrival patterns as the source depth changes.

With the basic responses as described above for reference, we can now proceed to analyze representative examples of the recorded field GPR data. The following section contains examples for each of the main BGPR configurations, and also, GPR data acquired on a line along the earth's surface between the two holes.

4. Field GPR data acquisition, processing, and interpretation

4.1. Site description

The field site (Coyote Basin) is located at the west side of the San Rafael Swell in east-central Utah (Fig. 7). It is in the upper portion of the Ferron Sandstone (Garrison et al., 1997), which is a clastic wedge within the Mancos Shale, that prograded into the Cretaceous Interior Seaway. The upper part of the Ferron is a thick fluvial-deltaic complex deposited during a rising sea level.

The physical configuration of the studied site is a planar mesa top adjacent to an east-facing cliff face. The sequence exposed in the cliff face is $\sim$12-m thick and consists of two main fluvial channel deposits lying above a floodplain mudstone (Corbeanu et al., in press). The upper 5–6 m contain medium-grained, trough cross-bedded sandstone, and the lower 7 m contain fine-grained, parallel laminated sandstone; see the lithology logs in Fig. 8. Thin clay drapes are common throughout the section, and clay clast conglomerates lie discontinuously upon the main bounding surfaces. The sand/clay interfaces generally produce good GPR reflections. The overall clay content increases substantially below 5–6-m depth, and produces rapid attenuation of the GPR signals.

The site contains extensive near-vertical fractures (Fig. 7). The main effect of these fractures in the present context is to introduce anisotropy into the GPR propagation velocity (as described below). In the larger context, the fractures would dominate the fluid permeability, but that is beyond the scope of the present paper. The presence of pore water can significantly change the relative dielectric permittivity, but the ambient water saturation is extremely low in this desert environment. The water table is at an unknown (but very great) depth throughout the region.

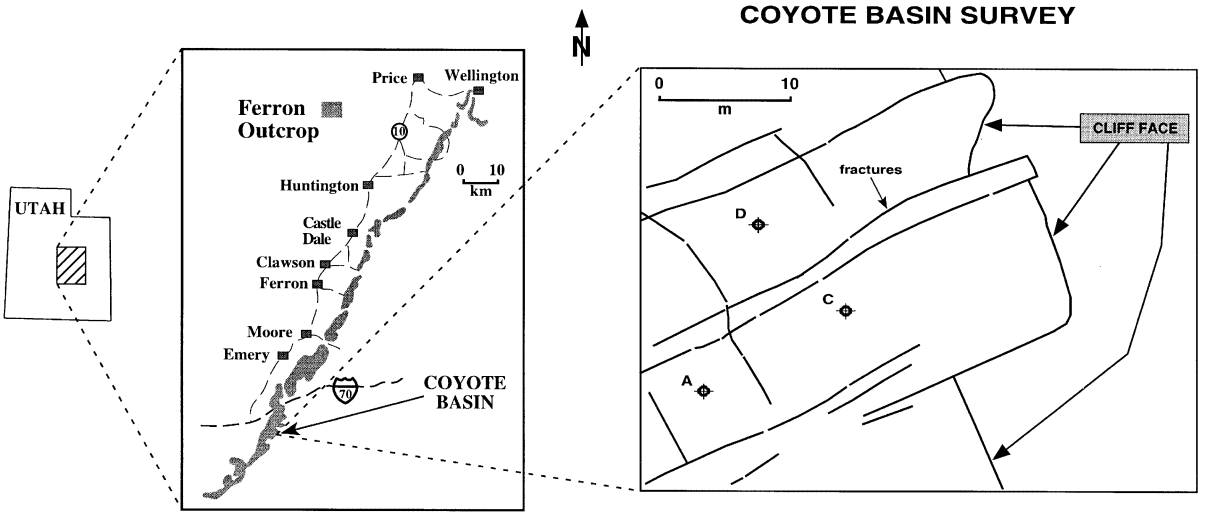

Fig. 7. Site location map. Utah is in the west central United States. A, C, and D in the rightmost panel are the locations of the boreholes used in this study. All panels are plan views.

4.2. Borehole GPR data acquisition and preprocessing

At Coyote Basin, three of the cored holes (A, C, and D) were close enough to each other (Fig. 7) to be used in cross-hole GPR surveys. The inter-hole spacings were 8.5 m (between holes D and C), 10.75 m (between C and A) and 12.75 m (between D and A). Usable hole depths were 12.5 m in A, 13.75 m in D, and 12.5 m in C.

All the BGPR data acquisition used 100-MHz half-wave dipole antennas, with a 1000-V transmitter. The time sample increment was 800 ps, the total recording time window was 600 ns to ensure that no usable signal was lost (only $\sim 250-300$ ns contained useful data), and 64 traces were stacked at each recording location to improve the signal-to-noise ratio. The positions of the antennas down the holes were controlled by distance marks on the borehole cables. Positions along the earth's surface were controlled by measuring tapes stretched between the holes. The surface topography along the lines was measured in a leveling survey. The boreholes are close to vertical and they are too short to contain any significant deviations. The time of the transmitter excitation was determined for each group of traces by recording a reference signal between the relevant pair of boreholes in the air (i.e., for the known distance and velocity) to define the true relative time zero; as this was done for each group of traces, any long period time drifts are automatically corrected.

A series of BGPR measurements were made with the following rationales.

(1) Vertical profiles were performed to measure vertical propagation velocity at each hole. The vertical profiles are useful for time-to-depth conversion of the surface GPR data collected on lines connecting the holes, and for correlation between the cores (and core measurements) and the GPR data.

(2) Three common-depth profiles were performed, one between each pair of the three holes, to measure the average horizontal velocity at each depth. This, combined with the vertical profile data, allows a direct measurement of velocity anisotropy.

(3) Complete suites of common-source tomographic data were collected between each pair of the three holes. These consisted of both cross-hole and hole-to-surface measurements. In this paper, representative examples are modeled; the tomographic imaging (for distributions of both velocity and attenuation on vertical slices between the holes) will be presented elsewhere. The model derived here may be used as the starting model for tomography.

(4) Common-offset surveys were collected on lines along the earth's surface between each pair of holes, to tie the borehole data together. The borehole data

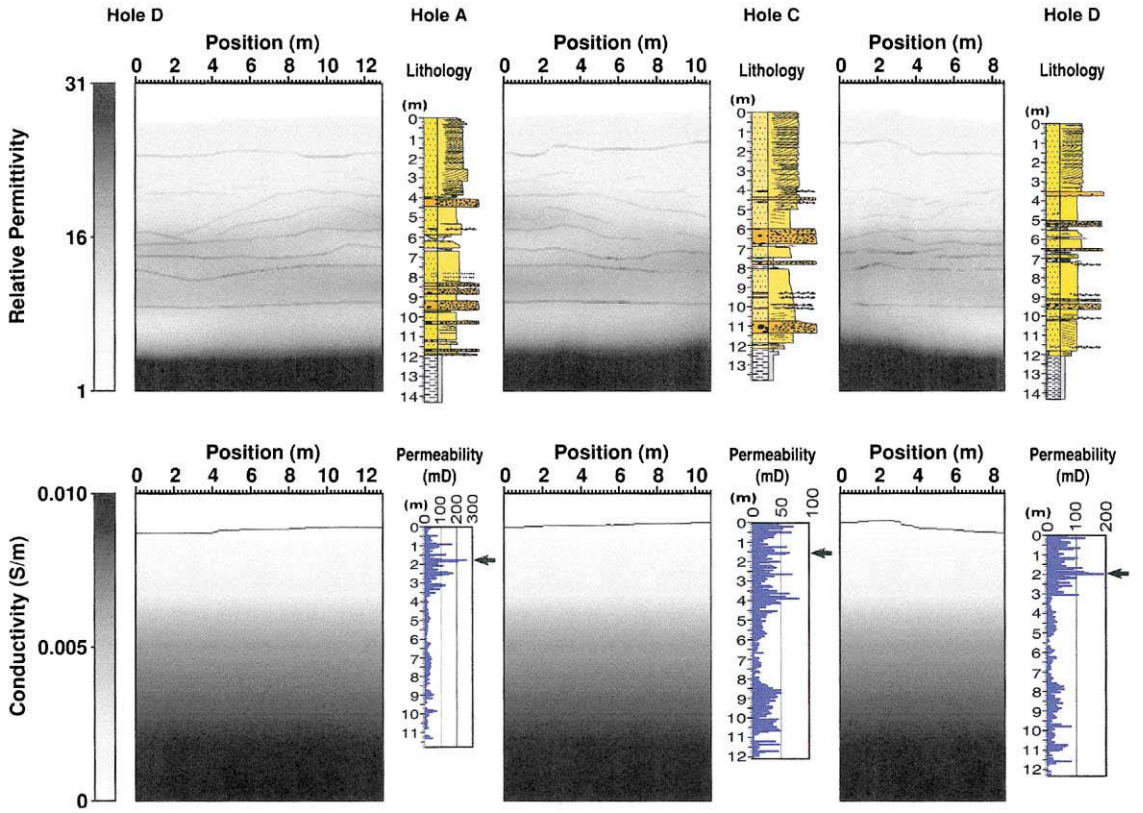

Fig. 8. Distributions of relative dielectric permittivity (above) and electrical conductivity (below) used to simulate the field data between hole pairs D–A (left panels), A–C (center panels) and C–D (right panels). These are obtained by iterative fitting of the data; see Figs. 9–14. Also shown are the lithology and fluid permeability logs from the holes. The depth scales on the logs also apply to the adjacent lithology/permeability plots. Depths are from the air–earth interface; depths less than zero correspond to air. In the lithology logs, yellow is sandstone, orange is clay intraclast conglomerate, and gray is mudstone.

(including core logs of the lithology, and porosity and permeability measurements) are the basis of the interpretation of the BGPR data.

Data processing consisted of time and exponential baseline corrections, trace editing, insertion of the elevation data into the trace headers, scaling to compensate for 3-D geometrical spreading (see details above), and bandpass filtering. Automatic gain control was applied for some of the displays (only) to enhance visibility.

4.3. Synthesis of field borehole GPR data

In this section, each of the BGPR data types (vertical, common-depth, tomographic, and surface profiles) will be considered in turn. Each data type will be presented with comparative analysis of the field and synthetic data.

The model used to generate the synthetic data for all examples is shown in Fig. 8. Distributions of both relative permittivity and electrical conductivity were determined by iterative fitting; model parameters were systematically perturbed to gradually improve the fit between the field and synthetic data. Approximately 50 iterations were performed. The model shown does not indicate the anisotropy of the velocity (obtained from the dielectric permittivity) that was measured (as shown below); the plotted permittivity corresponds to vertical propagation (i.e., horizontal polarization).

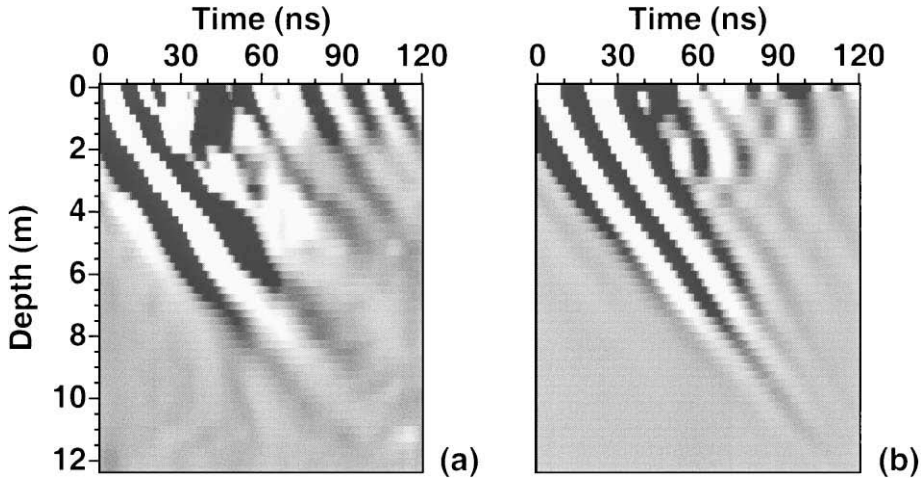

Fig. 9. Representative field (left) and synthetic (right) vertical radar profiles for hole A.

Vertical profiles were run in each of the three holes. This involved fixing one antenna at the top of the hole, and moving the other, from the bottom of the hole to the top, in 25-cm steps (see ray 8 in Fig. 2a). Fig. 9 shows the field and synthetic data for the vertical profile in hole A. Increasing depth corresponds to increasing time. The slope of the direct wave at any depth gives the vertical velocity of the local lithology at that depth. There is clearly a change in velocity (as seen in the slope of the direct wave) and in the attenuation (as seen in the reduced amplitude) below depths of $\sim 5-6$ m, which corresponds to the lithology change at this depth as described above (Fig. 8).

Fig. 10 shows the common-depth profile between holes D and A. In this survey, the antennas were moved together in 25-cm steps with both antennas at the same depth for each recorded trace (see rays in Fig. 2c). Here, the arrival time of the direct wave between holes is inversely proportional to the average horizontal velocity between the holes. The signal is difficult to follow in the high attenuation region below ~ 5-m depth. The signal can be followed to

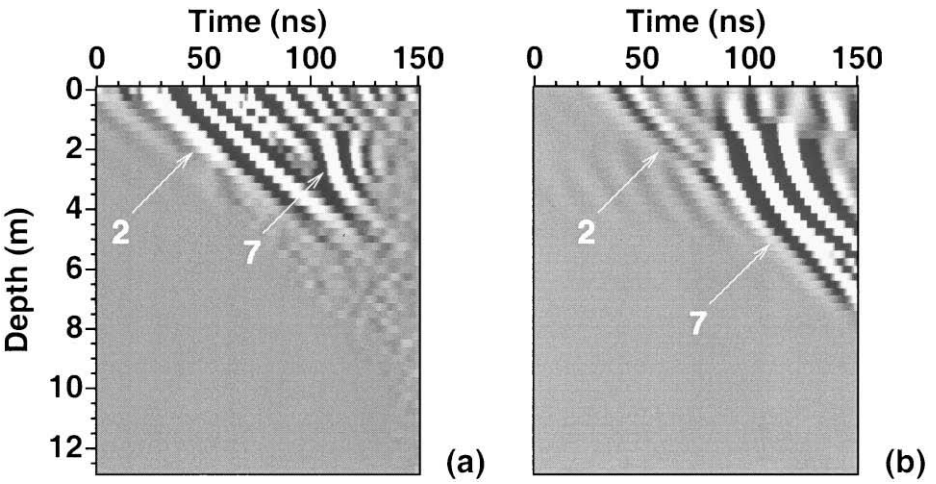

Fig. 10. Representative field (left) and synthetic (right) common-depth radar profiles between holes D and A. Energy labeled 2 corresponds to a critical refraction in the air at the earth's surface; energy labeled 7 is the direct wave between holes traveling in the rock (refer to Fig. 2. Some low amplitude ringing at early times in the synthetic data (b) is a filter artifact.

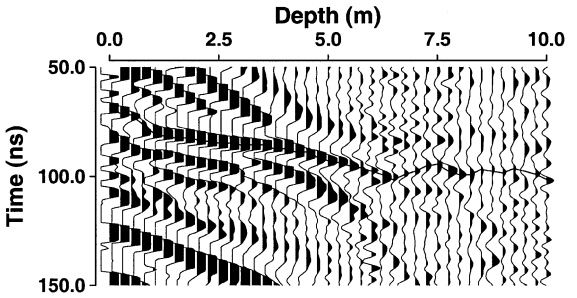

Fig. 11. Expanded view of the common-depth data between holes D and C. The solid line superimposed on the data indicates the traveltime picks used to compute the profile of average horizontal velocity at each depth; see Fig. 12. Time picking is facilitated by shifting the data forward in time so that the arrival time corresponds to the main (blackened) peak (which is easy to pick), rather than the pulse onset (which is not). Below ~8-m depth, the time picks are less reliable.

greater depth in the vertical profile (Fig. 9) because the path length in the attenuating layer is shorter than it is in the common-depth profile. Another point to note in Fig. 10 is that the first arriving wave at shallow depths is not the direct wave between holes (path 7 in Fig. 2) in the common-depth profile; rather, it is a critically refracted wave traveling in the air along the earth's surface (see path 2 in Fig. 2c). Thus, it may be sometimes difficult to pick arrival times of the direct wave accurately because of wave interference. Also note that the air waves are consistently larger in the field data than in the synthetics, because it is not possible, in a numerical model, to represent a sharp air–earth interface, and thus, the radiation pattern of the simulated antennas is not the same as that in the field data (especially in the horizontal direction). The match between the synthetic and field data is not as good in Fig. 10 as in most of the other figures, which we attribute mainly to unmodeled 3-D or frequency-dependent electromagnetic properties.

Fig. 11 shows an enhanced version of the common-depth data between holes D and C, and the picked direct wave travel times. The horizontal velocity is calculated from these times and the known distance

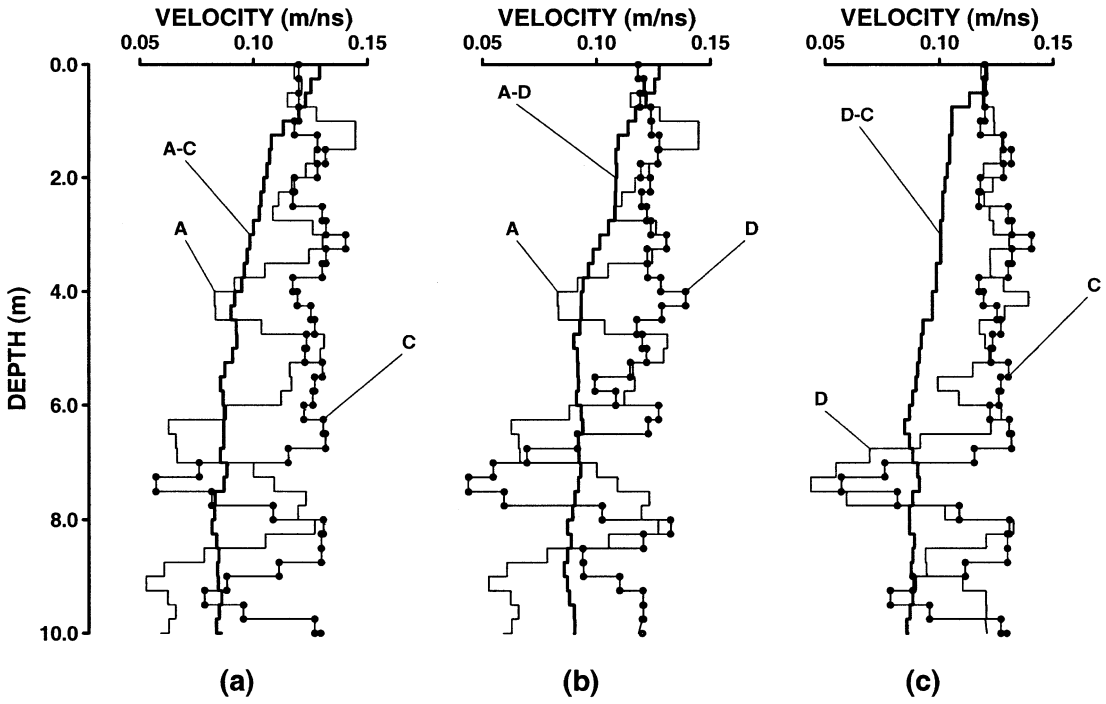

Fig. 12. Comparison of measured vertical and average horizontal velocities. (a) is for holes A and C, (b) is for holes A and D, and (c) is for holes D and C. In each panel, the heavy solid line is the average horizontal velocity between the pair of holes, and the two light lines are the vertical profiles for the two holes in the pair.

between the holes. Fig. 12 shows the velocity profiles estimated from each of the three common-depth profiles, along with the vertical velocity profiles from the holes at their ends. If the earth was isotropic, we would expect that the velocity profile from the common-depth survey between two holes would be similar to the average of those of the profiles from the two vertical surveys; this appears to be approximately true below 6-m depth (Fig. 12) but at shallower depths, where the time picks are more reliable (Figs. 10 and 11), the common-depth profiles are consistently biased to lower velocities, which indicates velocity

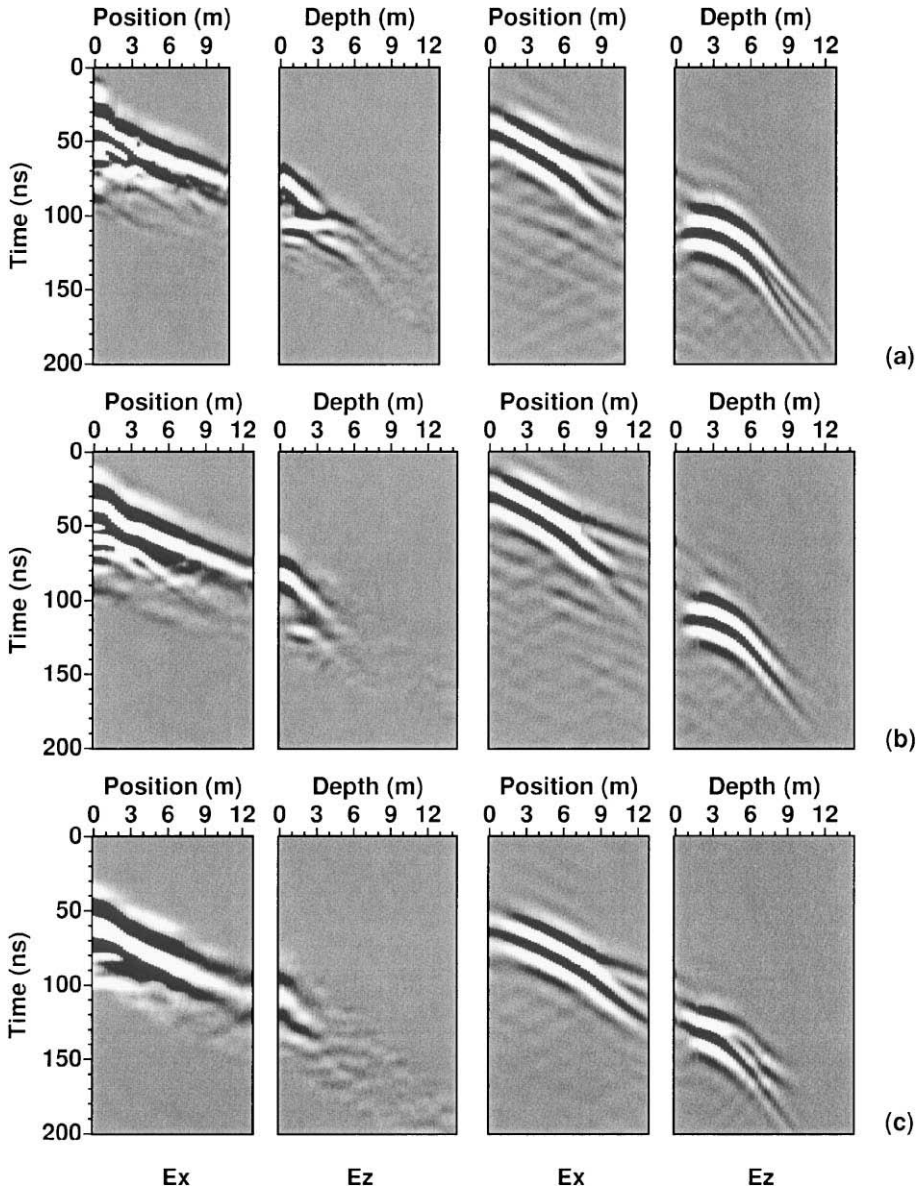

Fig. 13. Three representative tomographic common-source gathers. The two left columns are the field data and the two right columns are the synthetic data. For (a) and (b), the source is at 3.5-m depth in hole A; for (c), it is at 6.5-m depth in hole A. (a) is between holes A and C; (b) and (c) are between holes A and D. Some low amplitude ringing at early times in the synthetic data (b) is a filter artifact.

anisotropy; the average horizontal propagation is 20–25% slower than the vertical propagation. The main exception is in the upper 0.0–1.0 m where weathering probably distorts the original relations. The synthetic vertical profile in Fig. 9 was computed using 23% higher velocity than that corresponding to Fig. 8. The faster observed velocity in the vertical direction is contrary to that expected for horizontally layered media, if the anisotropy is caused by preferred horizontal orientation of the original depositional (or metamorphic) fabric (Tillard, 1994). At this site, we see two intersecting fracture sets (Fig. 7) with vertical orientations; these are the most likely cause of the observed anisotropy. The anisotropy is not visible at depths greater than 6 m (Fig. 12), which is consistent with fracture enhancement by weathering at the shallower depths. The presence of water may also enhance the differences in dielectric permittivity (Greaves et al., 1996; Sherman, 1986; Hubbard et al., 1997); there may be water adsorbed in the clays, even in this dry environment.

Full common-source tomographic gathers were acquired between hole pairs A–C, A–D, and D–C. These consisted of traces recorded every 25 cm in the receiver hole and across the surface to the top of the transmitter hole, for every transmitter position (Fig. 2b). The depth increment for the transmitter was also 25 cm. This provides a dense sampling of the vertical

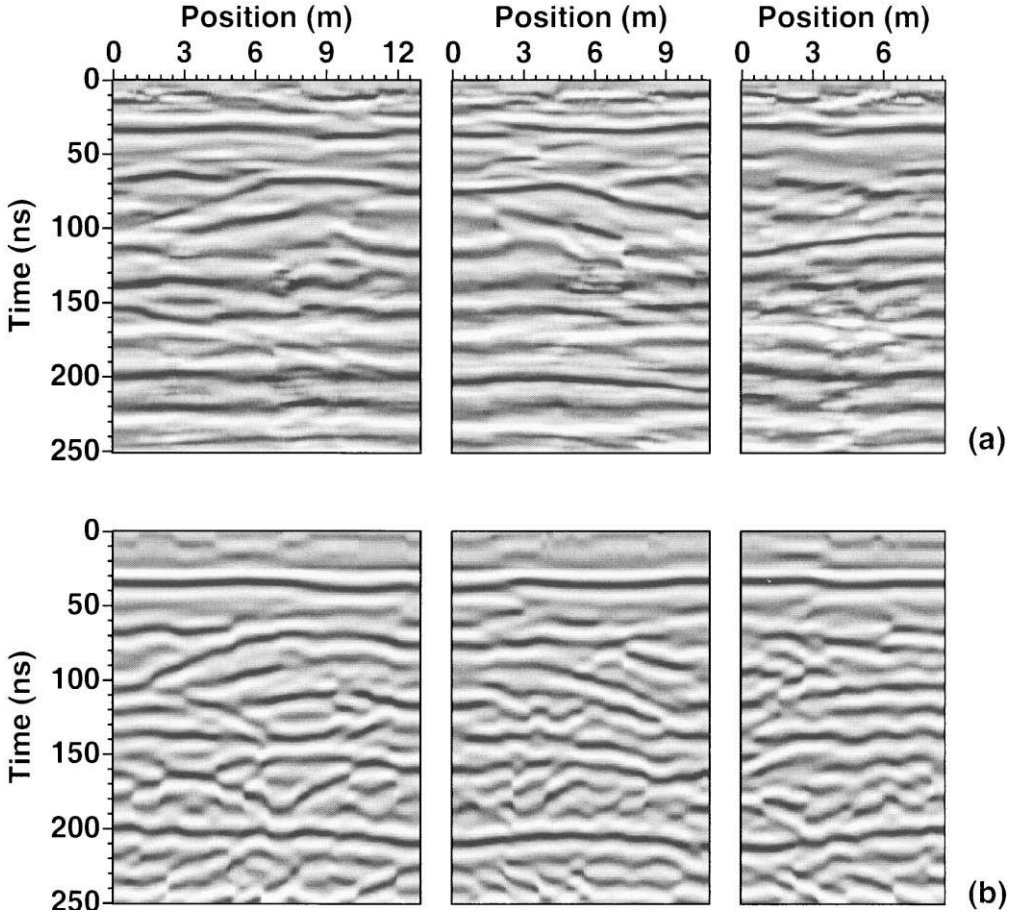

Fig. 14. Comparison of field (a) and synthetic (b) data for surface survey lines between the three hole pairs. The left panel is between holes D and A, the center panel is between holes A and C, and the right panel is between holes C and D (Fig. 7). Plots have automatic gain control with a time window of 30 ns. Compare with the true relative amplitude plots in Fig. 15.

slice between the holes. Fig. 13 shows three pairs of field/synthetic tomographic gathers; the main features of the field data are predicted by the synthetics, but there are details that are not fitted. The remaining misfits are assumed to be caused by differences between the 2-D isotropic model and the 3-D anisotropic real earth. Also note the amplitude and phase differences between the E_z and E_x fields, as illustrated in Fig. 6.

To assist in correlation of sedimentological and petrophysical data between the holes, and to study the details of the geometry of the structures present, high resolution common-offset GPR profiles were recorded on surface lines between the holes (see ray 5 in Fig. 2a), with antenna separation of 3 m and trace spacing of 10 cm. The corresponding field and synthetic data are shown in Figs. 14 and 15. In Fig. 14, the data are plotted with automatic gain control to emphasize the fitting of the reflection times via the relative permittivity distribution and reflector shapes (in the upper panels in Fig. 8). In Fig. 15, the same data are plotted with true relative amplitudes to emphasize the attenuation via the electrical conductivity distribution (in the lower panels in Fig. 8). The signal-to-noise level significantly decreases at times greater ~ 80 ns; attenuation decreases the signal strength and superposition of internal multiples and scattering increases the noise.

A comparison of the features in the model used to simulate the data, with the lithologic profiles at the holes (Fig. 8) does not show a perfect correspondence. For example, the continuous reflector at ~ 1.7-m depth (Fig. 8, upper panel) seems to occur in the middle of a thin-bedded sequence with no obvious

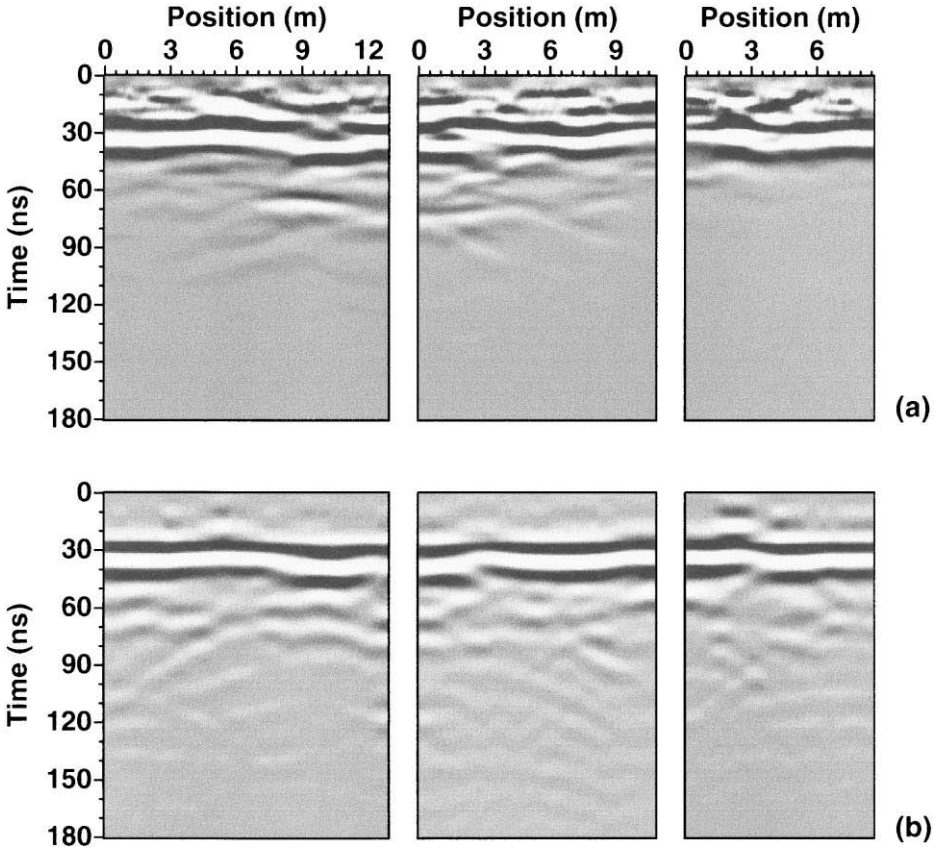

Fig. 15. Comparison of field (a) and synthetic (b) data for surface survey lines between the three hole pairs. The left panel is between holes D and A, the center panel is between holes A and C, and the right panel is between holes C and D (Fig. 7). Plots are true relative amplitude. Compare with the automatic gain control amplitude plots in Fig. 14.

major discontinuities. However, there is a direct correlation of this reflector with a layer of locally high fluid permeability (see the arrows in the lower panels of Fig. 8). Thus, all aspects that affect the electrical properties need to be considered in both model building and interpretation; both petrophysical and lithologic changes are potentially important. Local water saturation can also produce visible reflections, and is even more complicated as the water distribution may change with time. Percolation theory suggests that electrical conductivity should correlate with fluid permeability and water saturation, whereas the dielectric constant is determined more by the bulk rock properties as defined by porosity and total water content (e.g. Guéguen and Palciauskas, 1994).

The data above are representative of the data collected; the rest are similarly fitted by the same model (Fig. 8).

5. Synopsis and conclusions

Finite-difference modeling is shown to be a viable approach to simulation, analysis, understanding and interpretation of field BGPR data. Through synthesis of responses of models (of any desired complexity), the main arrivals can be identified and associated with their corresponding propagation paths. Iterative modeling can produce models of the spatial distributions of dielectric permittivity and electrical conductivity that are able to predict most of the main features, and even many of the subtleties, observed in field BGPR data. As the numerical modeling used was isotropic and 2-D, effects of anisotropy and 3-D structure could not be modeled; the remaining misfits between the field data and the simulations are attributed to these shortcomings. This provides incentive to expand the capability of the numerical modeling to be able to handle these directly.

Most previous studies of BGPR data used surveys located sufficiently below the surface to avoid the complications associated with the near-surface environment. In this study, we work from the air–earth interface downward. Thus, our simulations include internal multiple reflections from the air–earth interface and refractions, as well as the direct paths; this leads to complicated responses, even for simple models, but simulations also are a means of unraveling this complexity by viewing snapshots (Fig. 3) to see the origin of each wave in the model (Fig. 2). Imaging by prestack migration, which assumes that all arrivals are primary reflections, would not be as helpful in this context.

The geologic factors that control the distribution of GPR velocity and attenuation are lithology (especially clay content) and porosity/permeability (see the lithology and permeability logs in Fig. 8). Average estimated dielectric constants generally increase with depth from ~ 4 to ~ 17 in the sandy units, and are larger (as high as ~ 30) in the clays (Fig. 8). The corresponding estimated electrical conductivities are from 10^{-8} S/m for the most sandy layers to 10^{-2} S/m for the most clay-rich layers (Fig. 8). The high dielectric constants in the clays may be caused by adsorbed water.

Comparing the velocities for vertical and horizontal propagation of the electric fields shows a 20–25% anisotropy in the upper 6–7 m, with horizontal propagation faster than vertical; this is interpreted as being caused by the extensive vertical fracturing at the site (Fig. 7).

In the larger context of the whole project at Coyote Basin, the boreholes and cliff face sections provide the ground truth for all the (2-D and 3-D) GPR data. See Corbeanu et al. (in press) and Szerbiak et al. (2001) for more information. The structural geometry seen in the inter-hole surface survey profiles is consistent with the fluvial channel deposits exposed in the adjacent cliff face. These consist of medium-grained trough cross-bedded sandstone overlying fine-grained, parallel laminated sandstone. The information obtained here, when combined with permeability measurements can be the basis of a flow simulation.

Acknowledgements

The research leading to this paper was supported by the DOE under Contract DE-FG03-96ER14596, and by the sponsors of the UT-Dallas GPR Consortium. The GPR equipment used was a pulseEKKO IV system manufactured by Sensors & Software. Constructive comments by Karl Ellefsen and an anonymous reviewer are much appreciated. Dr. Xiaoxian Zeng assisted in the preparation of the final version of the figures. This paper is Contribution No. 946 from

the Programs in Geosciences at the University of Texas at Dallas.

References

Bergmann, T., Blanch, J.O., Robertsson, J.O.A., Holliger, K., 1999. A simplified Lax–Wendroff correction for staggered-grid FDTD modeling of electromagnetic wave propagation in frequency-dependent media. Geophysics 64, 1369–1377.

Cai, J., McMechan, G.A., 1995. Ray-based synthesis of bistatic ground-penetrating radar profiles. Geophysics 60, 87–96.

Cerjan, C., Kosloff, D., Kosloff, R., Reshef, M., 1985. A nonreflecting boundary condition for discrete acoustic and elastic wave equations. Geophysics 50, 705–708.

Corbeanu, R.M., Soegaard, K., Szerbiak, R.B., Thurmond, J.B., McMechan, G.A., Wang, D., Snelgrove, S.H., Forster, C.B., Menitove, A., 2001. Detailed internal architecture of a fluvial channel sandstone determined from outcrop, cores, and 3-D ground-penetrating radar: example from the Mid-Cretaceous Ferron Sandstone, east-central Utah. Bull. Am. Petrol. Geol. 85, 1583–1608.

Crase, E., Pica, A., Noble, M., McDonald, J., Tarantola, A., 1990. Robust elastic nonlinear waveform inversion: application to real data. Geophysics 55, 527–538.

Daniels, D.J., 1996. Surface Penetrating Radar. The Institution of Electrical Engineers, London.

Daniels, D.J., Gunton, D.J., Scott, H.F., 1988. Introduction to subsurface radar. IEE Proc. 135F, 278–320.

Davis, J.L., Annan, A.P., 1989. Ground penetrating radar for high resolution mapping of soil and rock stratigraphy. Geophys. Prospect. 37, 531–551.

Ellefsen, K.J., 1999. Effects of layered sediments on the guided wave in crosswell radar data. Geophysics 64, 1698–1707.

Garrison Jr., J.R., van den Bergh, T.C.V., Barker, C.E.F., Tabet, D.E., 1997. Depositional sequence stratigraphy and architecture of the Cretaceous Ferron Sandstone: implications for coal and coalbed methane resources—a field excursion. In: Link, P.K., Kowallis, B.J. (Eds.), Geol. Soc. Am., Field Trip Guidebook for the 1997 Annual Meeting, Part 2, pp. 155–202.

Gawthorpe, R.L., Collier, R.E.L., Alexander, J., Bridge, J.S., Leeder, M.R., 1993. Ground-penetrating radar: application to sandbody geometry and heterogeneity studies. In: North, C.P., Prosser, D.J. (Eds.), Characterization of Fluvial and Aeolian Reservoirs. The Geological Society, Special Publication, vol. 73, pp. 421–432.

Goodman, D., 1994. Ground-penetrating radar simulation in engineering and archeology. Geophysics 59, 224–232.

Greaves, R.J., Lesmes, D.P., Lee, J.M., Toksoz, M.N., 1996. Velocity variations and water content estimated from multi-offset ground-penetrating radar. Geophysics 61, 683–695.

Guéguen, Y., Palciauskas, V., 1994. Introduction to the Physics of Rocks. Princeton Univ. Press, Princeton.

Holliger, K., Bergmann, T., 1999. Finite-difference modeling of borehole georadar data. Soc. Expl. Geophys., 69th Annual Meeting, Expanded Abstracts, 457–460.

Holloway, A.L., Stevens, K.M., Lodha, G.S., 1992. The results of surface and borehole radar profiling from permit area B of the Whiteshell research area, Manitoba, Canada. 4th Internat. Conf. on GPR, Geol. Surv. of Finland, Spec. Pap., vol. 16, 329–337.

Hubbard, S.S., Rubin, Y., Majer, E., 1997. Ground-penetrating-radar-assisted saturation and permeability estimation in bimodal systems. Water Resour. Res. 33, 971–990.

Keller, G.V., 1987. Rock and mineral properties. In: Nabighian, M.N. (Ed.), Electromagnetic Methods in Applied Geophysics. Soc. Expl. Geophys., vol. 1, pp. 13–51.

Loucks, R.G., Mescher, P., McMechan, G.A., 2001. Characterizing the three-dimensional architecture of a coalesced, collapsed paleocave system in the Lower Ordovician Ellenburger Group by integrating ground-penetrating radar, shallow-core, and outcrop data (abstract). 2001 AAPG Annual Convention, June 3–6, Denver, USA.

McMechan, G.A., Soegaard, K., 1998. Sedimentological and geophysical studies of clastic reservoir analogs: methods, applications and development of ground-penetrating radar for determination of reservoir geometries in near-surface settings. Annual Report to the U.S. Dept. of Energy, Contract No. DE-FG03-96ER14596. The University of Texas at Dallas.

McMechan, G.A., Gaynor, G.C., Szerbiak, R.B., 1997. Use of ground-penetrating radar for 3-D sedimentological characterization of clastic reservoirs. Geophysics 62, 786–796.

Mur, G., 1981. Absorbing boundary condition for finite-difference approximation of the time-domain electromagnetic field equations. IEEE Trans. Elect. Comp. EMC-23, 377–382.

Olhoeft, G.R., 1988. Interpretation of hole-to-hole radar measurements. Proc., Third Tech. Symp. on Tunnel Detection, January 12–15, 1988. Golden, CO, 616–629.

Olsson, O., Falk, L., Forslund, O., Lundmark, L., Sandberg, E., 1992. Borehole radar applied to the characterization of hydraulically conductive zones in crystalline rock. Geophys. Prospect. 40, 109–142.

Petropolis, P.G., 1994. Stability and phase error analysis of FD-TD in dispersive dielectrics. IEEE Trans. Antennas Propag. 42, 62–69.

Reynolds, J.M., 1997. An Introduction to Applied and Environmental Geophysics. Wiley, New York, pp. 681–749.

Sherman, M.M., 1986. The calculation of porosity from dielectric constant measurements: a study using laboratory data.The Log Analyst, January–February, 15–24.

Siggins, A.F., 1992. Limitations of shallow cross-hole radar investigations. 4th Internat. Conf. on GPR, Geol. Surv. of Finland, Spec. Pap., vol. 16, pp. 307–315.

Szerbiak, R.B., McMechan, G.A., Corbeanu, R.M., 2001. 3-D characterization of a clastic reservoir analog: from 3-D GPR data to a 3-D fluid permeability model. Geophysics 66, 1026–1037.

Tillard, S., 1994. Radar experiments in isotropic and anisotropic geological formations (granite and schists). Geophys. Prospect. 42, 615–636.

Xu, T., McMechan, G.A., 1997. GPR attenuation and its numerical simulation in 2.5 dimensions. Geophysics 62, 403–414.

Zeng, X., McMechan, G.A., Cai, J., Chen, H., 1995. Comparison of ray and Fourier methods for modeling monostatic ground-penetrating radar profiles. Geophysics 60, 1727–1734.